IEEE Sensors Letters VOL. 9, NO. 2, FEBRUARY 2025 2500904 IEEE Sensors Council

Magnetic sensors

Impulsive Magnetic Anomaly Detection At the 100-m Scale With an Array of Induction Coil Magnetometers

Joonas A. Iivanainen[1,2], Timothy S. Read[1], Xianjin Yang[3], William Junor[4], and Daniel A. Thrasher[1]

[1] *Sandia National Laboratories, Albuquerque, NM 87123 USA*
[2] *Department of Neuroscience and Biomedical Engineering, Aalto University School of Science, FI-00076 Aalto, Finland*
[3] *Lawrence Livermore National Laboratory, Livermore, CA 94550 USA*
[4] *Los Alamos National Laboratory, Los Alamos, NM 87545 USA*

Manuscript received 1 October 2024; revised 13 November 2024; accepted 4 December 2024. Date of publication 11 December 2024; date of current version 8 January 2025.

Abstract—We demonstrate magnetic anomaly detection (MAD) using an array of 24 commercial induction coil magnetometers with stand-off distances from a pulsed 99.8(3) kA·m^2 magnetic dipole source of 260–1200 m. The sparse array is used to estimate the magnetic dipole location, magnitude, and orientation. We demonstrate how independent component analysis (ICA) improves the accuracy and precision of the magnetometer array when estimating the dipole parameters. Using sensor responses recorded from individual source pulses, we estimate the dipole location to within 29 ± 2 m, the magnitude to within 3 ± 3 kA·m^2, and dipole orientation error to within $19 \pm 0.6^\circ$.

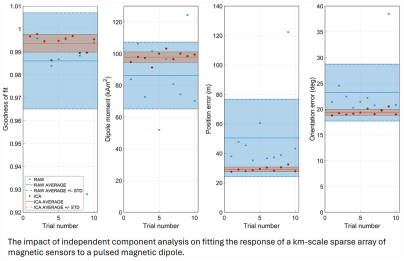

The impact of independent component analysis on fitting the response of a km-scale sparse array of magnetic sensors to a pulsed magnetic dipole.

Index Terms—Magnetic sensors, array-based sensing, independent component analysis (ICA), induction coil, magnetic anomaly detection (MAD).

I. INTRODUCTION

Magnetic anomaly detection (MAD) is the characterization of objects or events by their influence on detected magnetic fields (B-fields) [1]. MAD can be used to detect, locate and track hidden targets with magnetic signature, such as unexploded ordnance [2] and vehicles [3]. MAD has been used widely in many applications, such as in nondestructive industrial testing [4], geological surveys [5], and naval mine countermeasures tasks [6].

MAD has been demonstrated using both a single sensor and an array of sensors; the advantage of the latter being the ability to simultaneously measure the magnetic field at multiple locations. This enables MAD of transient events and the rejection of ambient magnetic field noise to improve the signal-to-noise ratio (SNR). Array-based MAD is characterized by the number of sensors (N), the sensor spacing (S), and the distance of closest approach (DCA) from the source to the nearest sensor. The specifics of several prior array-based MAD demonstrations are summarized in Table 1.

Here, we perform MAD of a pulsed magnetic dipole source with a DCA of 259 m using a sensor array of 24 nonuniformly (100 m-scale) spaced commercial induction coil magnetometers. We use the sensor array to localize the dipolar source by estimating its parameters by "dipole fitting", where we compare the measured B-field reported by each magnetometer with the B-field produced by a simulated dipole. We perform dipole fitting on ten individual pulses (no averaging across pulses). By comparing the ten location, magnitude, and orientation values estimated from the data with their actual values, we characterize both the accuracy and precision of the magnetometer array. In addition, we utilize independent component analysis (ICA) [11] to reject spurious signals from the raw B-field measurements. We characterize how ICA-cleaned data improves both the accuracy and precision of the dipole fits. Compared to prior work, this is the first demonstration of array-based MAD with a DCA greater than 50 m and the first application of ICA on a magnetometer array with sensor spacing at the 100 m-scale.

TABLE 1. Array-Based MAD Demonstrations

Ref	N	S (m)	DCA (m)
[7]	7	15	50
[8]	2	1	41
[9]	42	125 000	N/A
[10]	32	15 000	N/A
This work	24	~ 100	259

N: number of sensors, S: separation of sensors, DCA: distance of closest approach.

II. EXPERIMENTAL SETUP AND METHODS

The experimental geometry is as follows. Eight stations (see Fig. 1) with three orthogonal single axis vector magnetometers (Phoenix Geophysics MTC-150) are installed at various distances from the source (see Table 2). Each station has one magnetometer oriented along east-west (x), one along north–south (y), and one along the vertical (z). The MTC-sensor is an induction coil magnetometer and has a bandwidth of 10 kHz and sensitivity of 10 fT/$\sqrt{\text{Hz}}$ at 5 kHz

Corresponding author: Daniel A. Thrasher (e-mail: dathras@sandia.gov).
Associate Editor: Mitradip Bhattacharjee.
Digital Object Identifier 10.1109/LSENS.2024.3515639

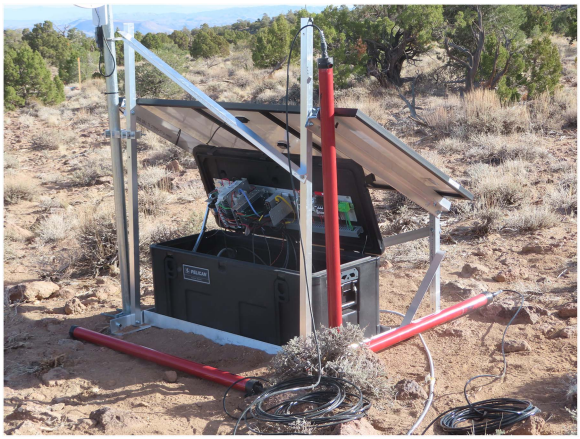

Fig. 1. Station hardware prior to installation. The red cylinders are the magnetometers. The black box contains the data recorder and batteries powered by the solar panel.

TABLE 2. Station Locations in Meters Relative to the Source Coil

Station	x	y	z	slant
PNADO	−319	283	242	490
PSAON	−42	−43	252	259
PSCIN	−141	−405	261	501
PWAOF	−104	59	255	282
PWBVI	−371	217	248	496
PWCES	−584	159	254	656
PWCTE	−852	212	279	921
PWDAM	−1159	184	308	1213

and 40 fT/$\sqrt{\text{Hz}}$ at around 10 Hz. The 144 cm × 7 cm sensor weights 6.4 kg.

The source is a custom coil with a radius of 2.0 m and height of 2.0 m with 24 turns and its axis of symmetry vertically oriented. A pulsed current supply drives current through the coil sufficient to produce a magnetic dipole with a 1 ms rise time and quasi-exponential decay time of ∼ 500 ms. The peak synthesized dipole moment is calculated from measurements of the current drawn through the coil and found to be 99.8(3) kA·m^2 .

We recorded 10 min of continuous raw temporal magnetometer data at 24 k samples/s/channel. We pulsed the source every 60 s giving in total ten pulses for the ten minute recording time. We use the open source Python toolbox MNE for signal processing of the magnetometer data [12]. MNE Python is developed for analyzing neurophysiological data from, e.g., magnetoencephalography (MEG) [13], but can nevertheless be applied to any multichannel time-series data. Using MNE Python, we bandpass filter the data to 0–1500 Hz before any of the analyses.

III. TEMPORAL DATA AND ICA

In this section, we show how ICA improves the data quality. In brief, ICA is a data-driven technique for transforming multiple sensor measurements via linear combinations into "components" that are maximally independent of one another. We use the MNE Python software to compute the ICA decomposition and to apply the ICA data reconstruction.

In total, 14 s of raw temporal data recorded by each of the 24 sensors is shown in Fig. 2 (left) (one sensor per trace). The timing of the pulsed source is shown using the vertical dashed lines. We see that the B-field measured by the sensors at the pulse time is strongly dependent on the stand-off, i.e., distance from the source to the sensor. The sensors also show unique B-field signatures at other times, which we attribute to local B-field interference. In addition, the sensors show B-field signatures that are independent of the sensor position (see for instance the data around $t = 4$ s). We attribute these common B-fields to distant lightning on account of their short duration and the fact that this data was acquired in the month of April in the Northern hemisphere when lightning is common.

Fig. 3 shows representative data around a single pulse after we rewrite the ten minute data set of 24 raw data signals in terms of 15 maximally independent components using ICA. We see that component ICA006 shows temporal dynamics most similar to our source, while components ICA000, ICA001, ICA008, and ICA011 show almost no similar pulse dynamics while also exhibiting large oscillatory behavior that we attribute to interference. We delete components ICA000, 001, 008, and 011 and reconstruct the 24 data channels without them.

Fig. 2 (right) shows the result of the ICA-cleaned data. We see that the B-field noise recorded by some sensors during the pulse times is improved. For example, the interference in sensor PWAOF-X is almost completely removed by ICA-cleaning thereby revealing the source pulse clearly. We also see that some B-field noise at other times is suppressed. However, some B-field noise signals (see for instance sensor PWCTE-Y) remain unsuppressed despite ICA-cleaning.

The average SNR for the raw data is 49 (range: 3–255) while for the ICA-cleaned data it is 91 (4–411). Over the channels, ICA improves the SNR by a factor of 5 on average (1–34); for the two X-oriented channels closest to the source (PWAOF-X and PSAON-X), ICA improves the SNR by factors of 9 and 34.

TABLE 3. Measured Mean and Standard Deviation of Fit Parameters From Ten Pulses for Raw and ICA-Cleaned Data

	Raw	ICA
Dipole moment (kA·m^2)	88(20)	98(3)
Position Error (m)	51(26)	29(2)
Orientation Error (deg)	23(6)	19.4(6)

IV. DIPOLE FITTING

In this section, we quantify the ability of the array to characterize the location, magnitude, and orientation of the source with and without ICA. We perform dipole fitting on the raw and ICA-cleaned data shown in Fig. 2 (right). The dipole fitting is performed using the FieldTrip software [14]. The dipole fitting algorithm assumes 1) uniform permeability between the source and the magnetometers, and 2) the source can be modeled as a magnetic dipole. The dipole fitting routine first performs a grid search using a grid over a volume of 1100 × 650 × 250 m^3 underneath the magnetometers. The grid comprises 1430 candidate sources with a distance of 50 m between adjacent sources. The candidate source with the greatest goodness of fit value is used as the starting location for nonlinear optimization. The nonlinear optimization yields the final estimate of the source parameters. We report the goodness of the fit, the estimated dipole moment, and the position and orientation errors of the dipole fit. The location error is defined as the Euclidean distance between the known source location and the fit estimate while the orientation error is the angle between the fit estimate and the known source orientation.

Table 3 shows the mean and standard deviations for three of the four fit parameters for raw and ICA-cleaned data, while Fig. 4 shows the corresponding box plots across the individual pulses for all four fit parameters. We see that the estimated dipole moments from fitting the

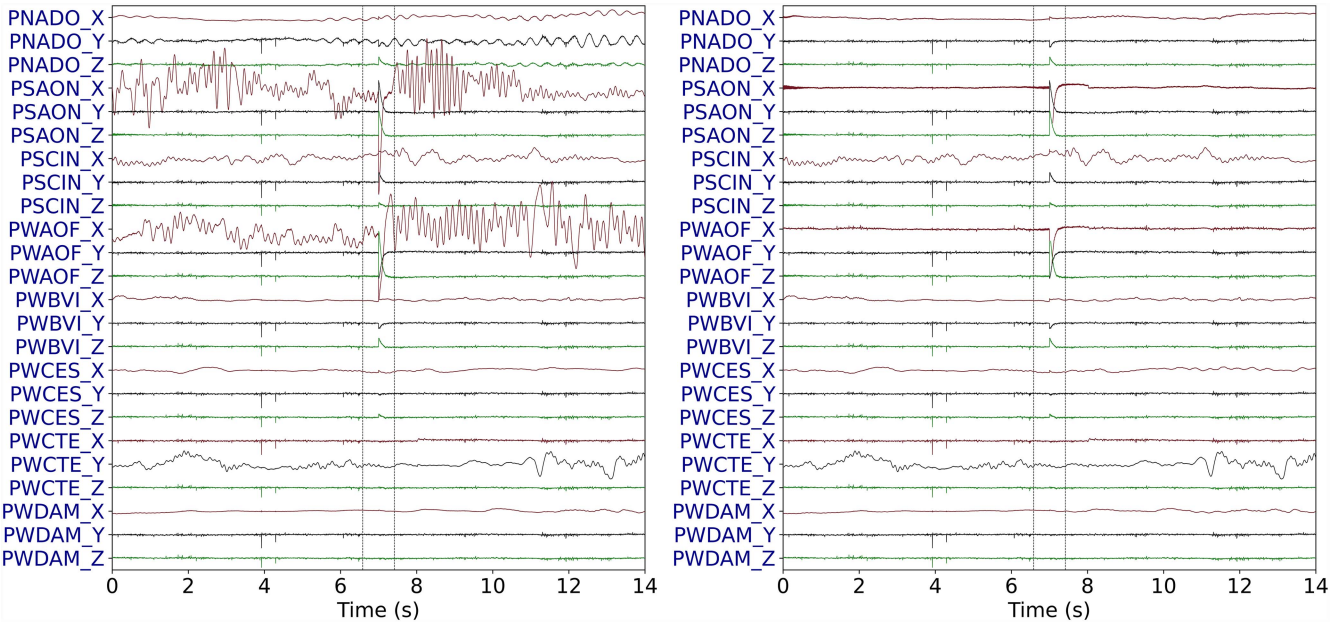

Fig. 2. Magnetometer data from 24 magnetometers before (left) and after (right) performing ICA to reject spurious signals. The vertical axes are all scaled the same (± 0.125 nT). The dashed vertical lines are centered around the time when the source is pulsed.

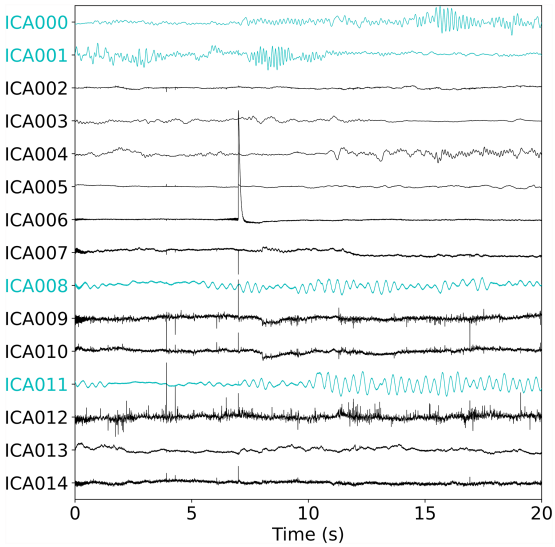

Fig. 3. ICA decomposition of the data from 24 induction coil magnetometers. The temporal behavior of 15 ICA components is shown for 20 seconds. The green channels were removed prior to reconstruction of the 24 signals.

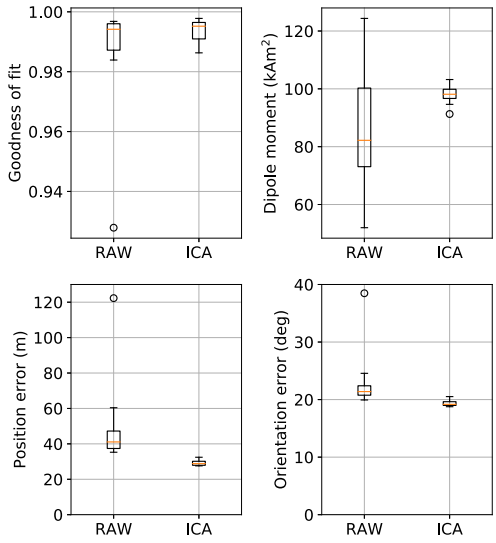

Fig. 4. Box plots of dipole fitting results of raw and ICA-cleaned data one pulse at a time. Data from all 24 magnetometer channels have been used.

raw and ICA-cleaned data agree with the dipole moment calculated from the current measured through the coil. We also see that ICA improves the accuracy (i.e., mean) and precision (i.e., standard deviation) of all fit parameters. We find that the fit solutions are offset in the same general direction relative to the actual source. We attribute the better localization accuracy of the ICA-cleaned data over the raw data to the increased SNR, especially in the two stations nearest to the source, which are critical in dipole fitting.

V. LIMITATIONS

We have shown that ICA roughly doubles the average SNR across the array allowing improved dipole fitting. We find that the ICA-cleaned sensor noise just prior to a pulse event is still 2 to 20× greater than the intrinsic noise estimated from the sensor data sheets. This suggests that even the ICA-cleaned data noise is not yet limited by the intrinsic sensor noise.

An incorrect permeability model of the medium between the sensors and the dipole source can limit the accuracy of the dipole fitting. For example, if the magnetic permeability at and above the location of the sensors is μ_0 while the magnetic permeability at the location of the source dipole and up to the sensors is μ then the dipole magnitude will be scaled by the factor $2\beta/(\beta+1)$, where $\beta = \mu/\mu_0$ [15]. If the permeabilities in the two regions are homogeneous then only the dipole

magnitude (and not measured dipole angle, orientation, and location) will be affected by β. However, an inhomogeneous permeability is likely to affect all of the estimated dipole parameters. In the experimental setup, the source coil was located in a chamber with a variety of ferrous material nearby, e.g., rock bolts and electrical conduit. It is thus very likely that our dipole-in-a-vacuum model does not properly account for the geophysical environment of the experiment thereby limiting the accuracy of the position and orientation estimates.

Other factors limiting the accuracy include sparse coverage of the sensor array and inaccuracies in the sensor scale factors (conversions from Volt to Tesla) and sensor orientations. For induction coil magnetometers, the scale factor depends on the area enclosed by the coil which can depend on many things, such as ambient temperature and mechanical deformation of the sensor. Sensor orientation accuracy is mostly dictated by the installation accuracy. Here, the sensors were installed with cm-scale accuracy over the roughly 100 cm sensor length, corresponding to an orientation uncertainty of roughly 0.6°.

To quantify the effects of scale factor and orientation errors on dipole fitting performance, we perform simulations where we introduce random deviations to the assumed sensor scale factors or orientations and then fit the data. These simulations show that for scale factor uncertainty $> 10\%$ and orientation uncertainty $> 4^\circ$ the fit-derived dipole position and orientation error both increase in statistically significant fashions. While the orientation uncertainty of the sensors installed in this work is likely less than the threshold for impacting the dipole fit, the scale factor uncertainty was similar to the threshold for impacting the dipole fit. Consequently, reducing the uncertainty of the scale factors of the sensors could improve the fit accuracy. The deployment of optically pumped magnetometers [16], the scale factors of which are much more certain compared to induction coil magnetometers, could enable improved dipole fit accuracy.

VI. CONCLUSION

We demonstrate MAD of a 100 kA·m^2 pulsed magnetic dipole using an array of 24 induction-coil magnetometers at eight different locations such that the source/sensor slant range varied from 260 to 1200 m. Even with our relatively sparse array, we estimate the dipole position within approximately 29 m and 19°. Moreover, we successfully applied ICA to denoise the data, which improved the dipole fitting results. We used the entire 10 min dataset to perform ICA but only information from the first pulse to determine which components to reject. The same components were rejected for subsequent pulse analysis.

We find that the accuracy of the dipole moment derived from fitting is limited by the fit precision, whereas the position and orientation accuracy derived from fitting are not. We have explored three possible sources of dipole position and orientation inaccuracy: sensor scale factor uncertainty, sensor orientation uncertainty, and spatial magnetic permeability uncertainty. We believe that scale factor uncertainty and spatial magnetic permeability uncertainty may limit the accuracy of the presented results.

ACKNOWLEDGMENT

This work was supported in part by the National Nuclear Security Administration, Defense Nuclear Nonproliferation Research and Development (NNSA DNN R&D) through Low Yield Nuclear Monitoring (LYNM) research, in part by the U.S. Government under Grant DE-AC05-76RL01830, and in part by the U.S. Department of Energy, National Nuclear Security Administration, through Mission Support and Test Services, operator of the Nevada National Security Site under Grant NA0003624.

The authors acknowledge important interdisciplinary collaboration with scientists and engineers from Los Alamos National Laboratory, Lawrence Livermore National Laboratory, Mission Support Technical Services, LLC, Pacific Northwest National Laboratory, and Sandia National Laboratories. Sandia National Laboratories is a multi-mission laboratory managed and operated by National Technology and Engineering Solutions of Sandia, LLC (NTESS), a wholly owned subsidiary of Honeywell International Inc., for the U.S. Department of Energy's National Nuclear Security Administration (DOE/NNSA) under contract DE-NA0003525. This written work is authored by an employee of NTESS. The employee, not NTESS, owns the right, title and interest in and to the written work and is responsible for its contents. Any subjective views or opinions that might be expressed in the written work do not necessarily represent the views of the U.S. Government. The publisher acknowledges that the U.S. Government retains a nonexclusive, paid-up, irrevocable, world-wide license to publish or reproduce the published form of this written work or allow others to do so, for U.S. Government purposes. The DOE will provide public access to results of federally sponsored research in accordance with the DOE Public Access Plan. This information has been authored by an employee or employees of the Triad National Security, LLC (LANS), operator of the Los Alamos National Laboratory under Contract No. 89233218CNA000001 with the NNSA, U.S. Department of Energy. Lawrence Livermore National Laboratory is operated by Lawrence Livermore National Security, LLC, for the U.S. Department of Energy, National Nuclear Security Administration under Contract DE-AC52-07NA27344.

REFERENCES

[1] Y. Zhao et al., "A brief review of magnetic anomaly detection," *Meas. Sci. Technol.*, vol. 32, no. 4, 2021, Art. no. 042002.

[2] Z. Zalevsky, Y. Bregman, N. Salomonski, and H. Zafrir, "Resolution enhanced magnetic sensing system for wide coverage real time UXO detection," *J. Appl. Geophys.*, vol. 84, pp. 70–76, 2012.

[3] S. V. Marshall, "Vehicle detection using a magnetic field sensor," *IEEE Trans. Veh. Technol.*, vol. 27, no. 2, pp. 65–68, May 1978.

[4] K. Kosmas and E. Hristoforou, "The effect of magnetic anomaly detection technique in eddy current non-destructive testing," *Int. J. Appl. Electromagn. Mechan.*, vol. 25, no. 1-4, pp. 319–324, 2007.

[5] S. Zhang, Z. Guan, J. Wang, and Y. Shi, "Detect adjacent well by analyzing geomagnetic anomalies," *Res. J. Appl. Sci., Eng. Technol.*, vol. 7, no. 11, pp. 2353–2361, 2014.

[6] R. Wiegert, B. Price, and J. Hyder, "Magnetic anomaly sensing system for mine countermeasures using high mobility autonomous sensing platforms," in *Proc. Oceans'02 MTS/IEEE*, 2002, pp. 937–944.

[7] L. Chen, Y. Feng, P. Wu, W. Zhu, and G. Fang, "An innovative magnetic anomaly detection algorithm based on signal modulation," *IEEE Trans. Magn.*, vol. 56, no. 9, Sep. 2020, Art. no. 6200609.

[8] L. Fan, C. Kang, H. Wang, H. Hu, X. Zhang, and X. Liu, "Adaptive magnetic anomaly detection method using support vector machine," *IEEE Geosci. Remote Sens. Lett.*, vol. 19, 2020, Art. no. 8001705.

[9] O. Kärhä and E. I. Tanskanen, "Newly digitized data from Scandinavian magnetometer array network shows large regional differences in magnetic environment," *J. Geophys. Res. Space Phys.*, vol. 127, no. 5, May 2022, Art. no. e2022JA030311.

[10] M. R. Ingham, D. K. Bingham, and D. I. Gough, "A magnetovariational study of a geothermal anomaly," *Geophys. J. Int.*, vol. 72, no. 3, pp. 597–618, Mar. 1983.

[11] A. Hyvärinen and E. Oja, "Independent component analysis: Algorithms and applications," *Neural Netw.*, vol. 13, no. 4-5, pp. 411–430, 2000.

[12] A. Gramfort et al., "MEG and EEG data analysis with MNE-Python," *Front. Neurosci.*, vol. 7, 2013, Art. no. 267.

[13] M. Hämäläinen, R. Hari, R. J. Ilmoniemi, J. Knuutila, and O. V. Lounasmaa, "Magnetoencephalography—theory, instrumentation, and applications to noninvasive studies of the working human brain," *Rev. Modern Phys.*, vol. 65, no. 2, 1993, Art. no. 413.

[14] R. Oostenveld, P. Fries, E. Maris, and J.-M. Schoffelen, "FieldTrip: Open source software for advanced analysis of MEG, EEG, and invasive electrophysiological data," *Comput. Intell. Neurosci.*, vol. 2011, pp. 1–9, 2011.

[15] J. D. Jackson, "Classical electrodynamics," 3rd ed., Hoboken, NJ, USA: Wiley, 1988, Art. no. 229.

[16] D. Budker and M. Romalis, "Optical magnetometry," *Nature Phys.*, vol. 3, no. 4, pp. 227–234, 2007.